Deep SCNN-based Real-time Object Detection for Self-driving Vehicles Using LiDAR Temporal Data

Shibo Zhou
Department of Electrical and Computer Engineering, Binghamton University, The State University of New York, Binghamton, NY, U.S.A., 13902, szhou19@binghamton.edu

Ying Chen*
Department of Management Science and Engineering, School of Management, Harbin Institute of Technology, China, 150000, yingchen@hit.edu.cn

Qiang Ye
Department of Management Science and Engineering, School of Management, Harbin Institute of Technology, China, 150000, yeqiang@hit.edu.cn

*corresponding author

Abstract

Real-time accurate detection of three-dimensional (3D) objects is a fundamental necessity for self-driving vehicles. Traditional computer-vision approaches are based on convolutional neural networks (CNN). Although the accuracy of using CNN on the KITTI vision benchmark dataset has resulted in great success, few related studies have examined its energy consumption requirements. Spiking neural networks (SNN) and spiking-CNNs (SCNN) have exhibited lower energy consumption rates than CNN. However, few studies have used SNNs or SCNNs to detect objects. Therefore, we developed a novel data preprocessing layer that translates 3D point-cloud spike times into input and employs SCNN on a YOLOv2 architecture to detect objects via spiking signals. Moreover, we present an estimation method for energy consumption and network sparsity. The results demonstrate that the proposed networks ran with a much higher frame rate of 35.7 fps on an NVIDIA GTX 1080i graphical processing unit. Additionally, the proposed networks with skip connections showed better performance than those without skip connections. Both reached state-of-the-art detection accuracy on the KITTI dataset, and our networks consumed an average (low) energy of 0.585 mJ with a mean sparsity of 56.24%.

Keywords: spiking-convolutional neural network, LiDAR temporal data, energy consumption, real-time object detection

1. Introduction

In recent years, increasing attention has been paid to point-cloud processing for autonomous driving because of significant improvements in automotive light detection and ranging (LiDAR) sensors, which deliver three-dimensional (3D) point clouds of the environment in real time. In contrast to images, LiDAR point clouds are unordered and sparse, resulting in some difficulties in real-time data use. However, they have highly varied density distributions throughout the measurement area (Qi et al. 2016). This provides potential solutions for 3D object detection (Chen et al. 2017, Wang and Posner 2015, Ku et al. 2017).

In the literature, to address 3D point-cloud challenges, many approaches have been proposed; they can be divided into three general classes. The first class projects point clouds into a perspective view; then it detects the object via image-based feature extraction (Premebida et al. 2014 and Gonzalez et al. 2015). The second class converts point clouds into a 3D voxel grid and uses hand-crafted features to encode each voxel (Wang and Posner 2015 and Engelcke et al. 2017). The third class is similar to the second but changes the hand-crafted features into machine-learned features (Girshick et al. 2014 and Krizhevsky et al. 2012). Owing to the machine-learned features, object detection can achieve significant performance. Based on this third class, Qi et al. (2016) proposed the PointNet method to learn the point-wise features of point clouds using deep neural networks. Qi et al. (2017a) proposed PointNet++ to allow networks to learn local structures at different scales. Most recently, Zhou and Tuzel (2018) developed the VoxelNet method, which can learn discriminative feature representations from point clouds and predict accurate 3D bounding boxes in an end-to-end module. Simon et al. (2018) developed Complex-YOLO, a real-time 3D object detector that uses an enhanced region-proposal network (E-RPN) to estimate the orientation of objects coded with imaginary and real parts for each box. Recently, Simon et al. (2019) presented a

novel fusion (i.e., Complexer-YOLO) of neural networks that uses a state-of-the-art 3D detector and visual semantic segmentation in the field of autonomous driving. With benchmarking on the KITTI vision benchmark dataset (Geiger et al. 2012), the detection accuracy of the proposed models in the literature has been demonstrated. However, few authors have focused on the energy consumption requirements of their proposed models. In autonomous vehicles, the efficiency of network energy consumption directly affects the neuromorphic architecture and is as important as detection accuracy. Thus, if a model consumes excessive energy to achieve high detection accuracy, it degrades hardware performance and increases energy consumption.

From the literature, convolutional neural networks (CNN) are the most popular techniques for achieving real-time 3D-object detection (Simon et al. 2019, Zhou and Tuzel 2018). However, CNNs consume more energy than other models, including spiking neural networks (SNN), which are known for low energy consumption (Tavanaei et al. 2019). In object and image recognition fields, numerous studies have been conducted using SNNs, achieving high recognition accuracies (Mostafa 2018; Kheradpisheh et al. 2018). However, owing to the non-differentiability of spiking activities, most SNNs have difficulty in handling complex image recognition. Recently, Zhou et al. (2019) proposed a direct training-based spiking-CNN (SCNN) that could recognize the complicated CIFAR-10 dataset using much less energy than CNN while reaching the same state-of-the-art accuracy. Nevertheless, efficient SCNN methods have not yet been employed using KITTI 3D point clouds. The main challenge is translating 3D point-cloud data into a suitable format for SNNs or SCNNs. For object recognition, the input image is first converted into spike trains (i.e., signals generated by neurons for mutual communication) based on pixel intensity (Tavanaei et al. 2019) or encoded into spike times (Mostafa 2018). Therefore, if we can convert the 3D point-cloud data into images, the current SNN or SCNN models can handle object detection. However, such potential conversion-based methods are not straightforward because the conversion process of 3D point clouds into images is complicated.

In this study, similar to Simon et al. (2019) and Zhou and Tuzel (2018), we quantize the point cloud to a 3D voxel representation, which is likely to contain certain features of points that localize within a voxel. To directly use 3D point clouds as an input, we design an innovative data-preprocessing layer by adding time information to each voxel. Using this method, the spike times can be obtained, and the temporal coding method can be applied to simulate the input for SNNs or SCNNs. Then, based on the YOLOv2 architecture (Redmon et al. 2015), we exploit the SCNN model of Zhou et al. (2019) to detect and localize objects. Note that the SCNN used in this study is an end-to-end method that combines feature extraction and bounding-box prediction. Moreover, we provide a method to calculate the sparsity of the network to estimate energy consumption. Although the calculated energy consumption value might not be the same as the practical one, it is still meaningful and can be used to demonstrate whether a network is energy efficient.

We thus propose two models considering skip connections (SC). A model without SC is suitable for the current chips in use, and a model using SC is planned for future chips. We evaluated our developed networks on the bird's-eye view and 3D detection tasks provided by the KITTI benchmark. Experimental results show that our models run with a much higher frame rate of 35.7 fps on an NVIDIA GTX 1080i graphical processing unit. Additionally, the

detection accuracies for cars, pedestrians, and cyclists are shown to reach state-of-the-art accuracies. In some cases, the proposed model with SC is even better. Moreover, our proposed networks cost an average of only 0.585 mJ with a mean sparsity of 56.24%, which connotes the model's higher efficiency. The contributions of our work are as follows:

- We design a novel data preprocessing layer to add temporal information to each voxel.
- We use SCNN to detect and localize an object based on the YOLOv2 architecture for the KITTI benchmark.
- We provide a way to examine the sparsity and energy consumption of the network.

2. Model Architecture

As shown in Fig. 1, the proposed model comprises three functional blocks: a data preprocessing layer, feature-learning (spiking-convolutional) layers, and a detection layer. In the following sections, we provide a detailed introduction of the working of these three blocks.

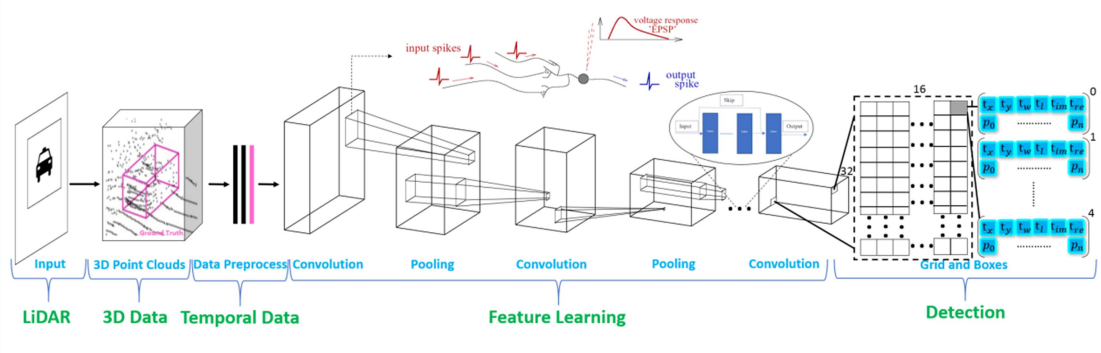

Figure 1. An example of the proposed object detection architecture

2.1. Point Cloud Preprocessing

For the 3D point cloud from KITTI, each point has the positional information, which can be represented by a 3D coordinate system. Similar to Simon et al. (2018), our region of interest in the point cloud is $[0,60]m \times [-40,40]m \times [-2.73,1.27]m$ in sensor coordinates. Therefore, if the laser emission equipment is the origin of the coordinate, the distance between each point and the laser emission equipment can be calculated as

$$d = \sqrt{x^2 + y^2 + z^2}, \tag{1}$$

where $x \in [0,60]$, $y \in [-40,40]$, and $z \in [-2.73,1.27]$. The laser device emits a pulse, which is sent back to the laser reception device after it is reflected from an object. Hence, the total time for the pulse from emission to reception is

$$t = \frac{2d}{v}, \tag{2}$$

where v is the speed of the laser pulse and t is the time information of each point. Next, we quantize the point clouds to a 3D voxel representation that contains certain features of the points located within the voxel. We choose a resolution of $768 \times 1024 \times 21$ with the size of each cell approximately equal to $0.08 \times 0.08 \times 0.19m$. Owing to this setting, each voxel exists with at least one point in its 3D space. If there is more than one point within a voxel, we randomly select one and use its time information to represent the voxel. As shown in Fig. 2, the voxelated space has a 3D coordinate system based on the resolution. Therefore, each voxel contains length (768), width (1024), height (21), and time information *t*, which can be regarded as spiking times that carry precise information. Consequently, we use the temporal coding method to encode the input information, *t*, for SCNN.

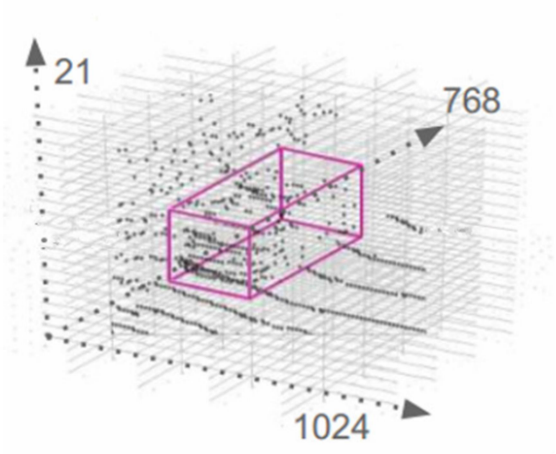

Figure 2. Voxelized point clouds within a 3D coordinate system.

2.2. Principle of SCNN

Following Mostafa (2018), in the spiking-convolutional layers, we used a non-leaky integrate and fire neurons with current exponentially decaying synaptic kernels. A neuron's membrane dynamics are described by

$$\frac{dV_{mem}^{j}(t)}{dt} = \sum_i w_{ji} \sum_r k(t - t_i^r), \tag{3}$$

where the right-hand side of Eq. (3) is the synaptic current, V_{mem}^{j} is the membrane potential of neuron j, w_{ji} is the weight of the synaptic connection from neuron i to neuron j, t_i^r is the time of the r^{th} spike from neuron i, and k is the synaptic current kernel given by

$$k(x) = \theta(x) exp(-\frac{x}{\tau_{syn}}) \; where \; \theta(x) = \begin{cases} 1 \; if \; x \geq 0 \\ 0 \; otherwise \end{cases}. \tag{4}$$

The synaptic current jumps immediately when an input spike arrives; then it decays exponentially with a time constant, τ_{syn}, which is set to 1 for the rest of this discussion. According to this mechanism, we assumed that a neuron receives *N* spikes at times $\{t_1, \ldots, t_N\}$

with weights $\{w_1, \ldots, w_N\}$ from N source neurons, and these spike times accumulate. As seen in Fig. 3, the neuron spikes when its membrane potential is over the firing threshold. After a spike, the membrane potential automatically resets to 0.

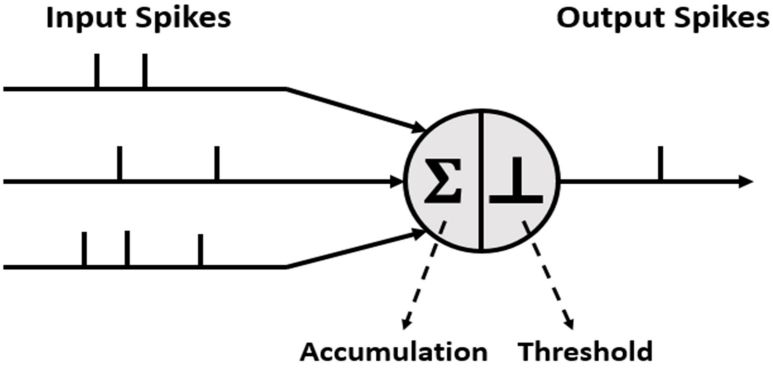

Figure 3. A model of spike neuron involved accumulation operation and threshold comparative.

If the neuron spikes at time t_{out}, the membrane potential for $t < t_{out}$ can thus be represented by

$$V_{mem}(t) = \sum_{i=1}^{N} \theta(t - t_i) w_i (1 - exp(-(t - t_i))). \quad (5)$$

t_{out} is then defined as

$$1 = \sum_{i \in C} w_i (1 - \exp(-(t_{out} - t_i))), \quad (6)$$

where "1" indicates the threshold and $C = \{i: t_i < t_{out}\}$. Eq. (6) indicates that when the right-hand side is greater than 1, the neuron will spike. Therefore,

$$exp(t_{out}) = \frac{\sum_{i \in C} w_i exp(t_i)}{\sum_{i \in C} w_i - threhold}. \quad (7)$$

The backbone network follows a YOLOv2 architecture (Redmon et al. 2015), used to process the spiking-time data. As mentioned, we used non-leaky integrate-and-fire neuron to implement the convolution process, and each convolution kernel comes from Eq. 7. Therefore, communication between convolutional blocks occurs entirely through the spike signal. The convolutional operation of this study is shown in Fig. 4 (Zhou et al. 2019). In short, prior to matrix multiplication, we sort the spiking-time values in the small square of the input data in layer *n,* from small to large, as vector *T*. The elements in the kernel matrix are reordered to generate *W* according to the changed position of spiking-time values. In terms of Eq. (7), for $w_i \in W$ and $t_i \in T$, a dot-product computation is performed between w_i and $\exp(t_i)$. The neuron fires when the accumulated dot products reach the threshold. Consequently, the value of the mapping element, t_{out}, becomes the output. As noted, after the neuron fires, it is not allowed to fire again. Because we use temporal coding, the fired spikes can be quite sparse because the time of each spike carries significant information. Combined with the real-time nature of YOLOv2, the presented network can be implemented more efficiently on a

neuromorphic architecture than on a traditional neural network.

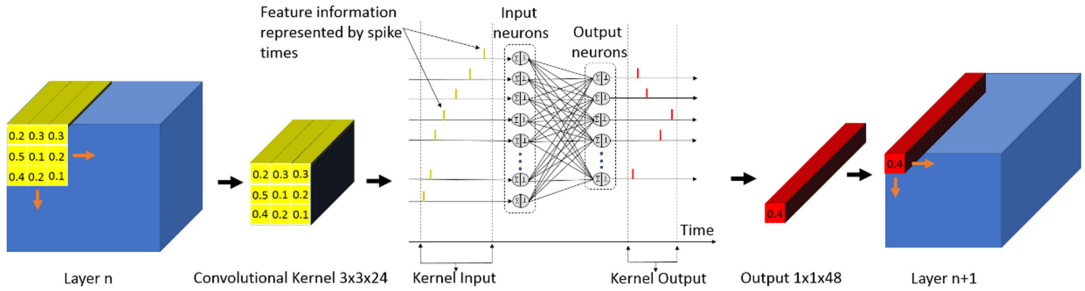

Figure 4. Spiking-convolutional process (kernel size: height × width × channels)

2.3. Detection and Regression

Following Simon et al. (2018), we used E-RPN to split the 3D position $b_{x,y}$ object dimensions (width b_w and length b_l), probability p_0, class scores $p_1 \ldots p_n$, and finally its orientation, $b_\emptyset$, from the incoming feature map. To achieve proper orientation, we exploited the updated Grid-RPN approach from Simon et al. (2018).

$$b_x = \sigma(t_x) + c_x, \tag{8}$$

$$b_y = \sigma(t_y) + c_y, \tag{9}$$

$$b_w = pwe^{t_w}, \tag{10}$$

$$b_l = p_l e^{t_l}, \tag{11}$$

$$b_\emptyset = arg(|z|e^{ib_\emptyset}) = arctan_2(t_{Im}, t_{Re}), \tag{12}$$

where t_{Im} and t_{Re} are the responsible regression parameters. With $arctan_2(t_{Im}, t_{Re})$, we can easily obtain the angle. Additionally, our regression parameters are directly linked to the loss function, L_{loss}, based on the Complex-YOLO of Simon et al. (2018). Specifically, the loss function is represented by

$$L_{loss} = L_{YOLO} + L_{Euler}, \tag{13}$$

where L_{YOLO} is the sum of squared errors using the introduced multi-part loss, as shown in Redmon et al. (2015). Additionally, according to Simon et al. (2018), the Euler regression part of the loss function, L_{Euler}, is defined as

$$L_{Euler} = \lambda_{coord} \sum_{s=0}^{S} \sum_{b=0}^{B} \alpha_{sb}^{obj} [(t_{im} - \hat{t}_{im})^2 + (t_{re} - \hat{t}_{re})^2], \tag{14}$$

where α_{sb}^{obj} indicates the b^{th} bounding-box predictor in cell s, which has the highest intersection over union (IoU) in comparison with the ground truth for that prediction; λ_{coord} is a scaling factor used to guarantee stable convergence during early phases; and $\hat{t}_{im}$ and $\hat{t}_{re}$ are the estimated responsible regression parameters.

3. Energy Consumption Calculation

Similar to Simon et al. (2018) and Zhou and Tuzel (2018), our network is a single-stage

detector that can be trained in an end-to-end manner. Hence, our proposed network also has a lower running time than other CNN models (Girshick 2015; Ren et al. 2015). Moreover, our network is more energy efficient because the network signals are transmitted via spikes.

For the spike-based information coding strategy, we used the scheme of the time-to-first-spike from Ponulak and Kasinski (2011). As seen in Eq. (6), the neuron spikes only when the membrane potential of the neuron reaches the threshold. After the neuron spikes, it is not allowed to spike again. To recognize the pattern or detect a scene, if the first N neurons from the input layer can cause a neuron of the next layer to spike, the rest of the M neurons in the input layer will not spike. This way, some neurons will not spike in each layer. Hence, we can calculate the sparsity of each layer using the following equation:

$$S_k = \frac{M_k}{M_k + N_k}, \tag{15}$$

where S_k is the sparsity of the k^{th} layer, N_k is the number of spiking active neurons in the k^{th} layer, and M_k is the number of non-active neurons in the k^{th} layer. The total sparsity of the network is

$$S_{total} = \frac{M_{total}}{M_{total} + N_{total}} = \frac{\sum_{k=1}^{K} M_k}{\sum_{k=1}^{K} M_k + \sum_{i=1}^{K} N_k}, \tag{16}$$

where M_{total} is the total number of non-active neurons, and N_{total} is the total number of active neurons. Hence, the total energy consumption of the network can be calculated as

$$P = N_{total} \times p, \tag{17}$$

where p is the energy consumed by each spike and P is the total energy consumed by the network.

4. Training and Experiments

In this section, we describe the proposed networks and their training for the evaluation of the KITTI data in details.

4.1. Training Details

We evaluated the proposed networks using the challenging KITTI object detection benchmark, which contained 7481 and 7518 samples for training and testing, respectively. Because the input was LiDAR data, we only focused on birds-eye-view and 3D object detection for cars, pedestrians, and cyclists. Similar to the literature, each class was evaluated based on three difficulty levels (i.e., easy, moderate, and hard), considering the object's size, distance, occlusion, and truncation. The detailed architecture of the proposed network is given in Table 1. In the last layer, we used a traditional convolutional layer instead of a spiking-convolutional layer because for SCNN, the input value was time information. Thus, negative values were not allowed. Second, the values of some coordinates of the real 3D LiDAR data were negatively based on the range presented in Section 2.1.1. Third, the traditional convolutional layers could handle the negative values of information with the activation function, $f(x) = x$. Finally, using the spiking-convolutional layer as the last layer gave very dismal results compared with the current ones from our preliminary test. Therefore, we decided to exploit the traditional convolutional layer as the last one.

Although the proposed network was based on the Complex-YOLO design from Simon et al. (2018), our network used only 9 spiking-convolutional layers, 1 traditional convolutional layer, 5 maxpool layers, and 3 intermediate layers, whereas Simon et al. (2018) used 18 convolutional layers, 5 maxpool layers, and 3 intermediate layers. Our proposed network was comparatively much simpler than that of Simon et al. (2018). From the perspective of energy consumption, the simpler the network architecture, the less energy the network will consume.

As introduced by He et al. (2015) and Orhan and Pitkow (2018), SCs are simply extra connections between nodes at different layers of a neural network that skip one or more layers of nonlinear processing. However, they can improve the training of very deep neural networks without changing their main structure. Hence, in our network, we used SC to improve the performance of our network. However, latest detection chips (e.g., HTPU from CORAL and Akida from BrainChip) do not support SC. The main reason is that the nodes of the hardware do not support event-packet synchronization across multiple layers. An SC also consumes extra energy in practice. Hence, we trained two models: one with and the other without SC.

The models were trained from scratch using stochastic gradient descent with a weight decay of 5e−4 and momentum of 0.9. The implementation was based on a modified version of the YOLOv2 framework (Redmon et al. 2015). Because the proposed model was a supervised learning-based network and the testing samples in the KITTI dataset had no labels, following the principles from Zhou and Tuzel (2018), Chen et al. (2016), and Simon et al. (2018), we divided the training set with an available ground truth and allocated 85% data for training and 15% for testing. To train the model well, during the first epoch, we started with a learning rate at 5e−5 to ensure convergence. After four epochs, we scaled the learning rate up to 5e−4 and gradually decreased it up to 1000 epochs.

Table 1. Detailed network information

Layer	filters	size	input	output
Spike-conv	32	3x3/1	768×1024×21	768×1024×32
max		2x2/2	768×1024×32	384×512×32
Spike-conv	48	3x3/1	384×512×32	384×512×48
max		2x2/2	384×512×48	192×256×48
Spike-conv	64	3x3/1	192×256×48	192×256×64
max		2x2/2	192×256×64	96×128×64
Spike-conv	128	3x3/1	96×128×64	96×128×128
max		2x2/2	96×128×128	48×64×128
Spike-conv	256	3x3/1	48×64×128	48×64×256
Spike-conv	1024	3x3/1	48×64×256	48×64×1024
Spike-conv	512	3x3/1	48×64×1024	48×64×512
max		2x2/2	48×64×512	24×32×512
Spike-conv	1024	3x3/1	24×32×512	24×32×1024
route	9			
reorg		/2	48×64×256	24×32×1024
route	13			

Spike-conv	1024	3x3/1	24×32×2048	24×32×1024
conv	75	1x1/1	24×32×1024	24×32×75
loss			**24×32×5×1 5**	

Based on Eq. (15), we obtained the sparsity of each layer. Consequently, we achieved the sparsity of the network for each sample using Eq. (16). There were 1122 samples for validation, and the minimum, maximum, and mean sparsity of our network is given in Table 2. As observed, for the two trained models, there is no major difference between the maximum and minimum sparsities. Additionally, the mean sparsity of the network is 56.24% for the KITTI dataset. Based on Merolla et al. (2011), each spike consumed 45 pJ. Accordingly, the energy consumption of the network was 0.585 mJ, because on average, the number of active neurons was ~13 million. Traditionally, all neurons are used for object detection or recognition. Thus, the energy consumption should be higher than the obtained one. As noted, the estimated energy consumption does not consider the energy spent in the last layer of the network. However, such a small value still connotes the energy efficiency of our proposed model.

Table 2. Network sparsity for the KITTI dataset

	Minimum	Maximum	Mean
Sparsity	54.08%	58.41%	56.24%

4.2. Experiments

We adjusted our experimental setup and followed the official KITTI evaluation protocol, where the IoU thresholds were 0.7 for the Car class, and 0.5 for Pedestrian and Cyclist classes. The IoU threshold was the same for both the bird's-eye view and full 3D evaluation. We compared the methods using the average precision (AP) metric.

Evaluation in the Bird's-Eye View. Our evaluation results for birds-eye-view detection are given in Table 2. Simon et al. (2018) compared their proposed model, Complex-YOLO, with the first five leading models presented in Table 2 and demonstrated that their model outperformed all five in terms of running time and efficiency. They were still able to achieve detection accuracy comparable with state of the art. As noted, although Complexer-YOLO (Simon et al. 2019) was more complicated than Complex-YOLO when considering more factors, the detection accuracies for all classes were lower than that of Complex-YOLO. Hence, we first focused on the comparison between Complex-YOLO and our model. As seen, all accuracies of our proposed model having SC for detecting the car, pedestrian, and cyclist were higher than those using Complex-YOLO. Although our frame rate was 35.7 fps, lower than the 50.4 fps of Complex-YOLO, it was still much higher than those of the other five models. Moreover, in terms of detection accuracy, at the easy, moderate, and hard cyclist levels, our proposed model reached higher accuracies than the others. Furthermore, our model without SC also reached state-of-the-art detection accuracy. However, it had slightly worse performance than that with SC.

Table 3. Performance comparison for birds-eye-view detection. APs (in %) for our experimental setup compared with existing leading models.

Method	Modality	FPS	Car			Pedestrian			Cyclist		
			Easy	Mod.	Hard	Easy	Mod.	Hard	Easy	Mod.	Hard
MV3D	LiDAR + Mono	2.8	86.02	76.90	68.49	-	-	-	-	-	-
F-PointNet	LiDAR +Mono	5.9	88.70	84.00	75.33	**58.09**	**50.22**	**47.20**	75.38	61.96	54.68
AVOD	LiDAR + Mono	12.5	86.80	**85.44**	77.73	42.51	35.24	33.97	63.66	47.74	46.55
AVOD-FPN	LiDAR + Mono	10.0	88.53	83.79	77.90	50.66	44.75	40.83	62.39	52.02	47.87
VoxelNet	LiDAR	4.3	**89.60**	84.81	78.57	65.95	61.05	56.98	74.41	52.18	50.49
Complex -YOLO	LiDAR	**50.4**	85.89	77.40	77.33	46.08	45.90	44.20	72.37	63.36	60.27
Our model with SC	LiDAR	35.7	86.54	81.97	79.11	50.27	48.21	46.47	**75.57**	**65.48**	**63.21**
Our model without SC	LiDAR	35.7	86.93	82.70	**82.23**	38.34	36.43	35.52	62.40	55.97	55.34

(Note: MV3D is from Chen et al. (2016), F-PointNet is from Qi et al. (2017b), AVOD is from Ku et al. (2017), AVOD-FPN is from Ku et al. (2017), VoxelNet is from Chen and Tuzel (2018), and Complex-YOLO is from Simon et al. (2018))

3D Object Detection. Apart from the birds-eye-view detector, we applied our proposed model to the full 3D object detector; the results are presented in Table 4. Similar to Simon et al. (2018), we did not directly estimate the height information with regression but instead used a fixed spatial height location extracted from ground truth to implement the 3D object detection. As seen in Table 4, the detection accuracies of our model with SC on the car, pedestrian, and cyclist were all better than those of Complex-YOLO. Additionally, the accuracies of the proposed model with SC were comparable with those of the other five models. Our model reached its highest accuracy with the moderate and hard cyclist levels. Moreover, the proposed model with SC in all cases showed better performance than those without SC, which also reached state-of-the-art accuracies. To illustrate the detection performance of our proposed model with SC, several 3D detection examples are presented in Fig. 5. For better visualization, we projected 3D boxes detected using LiDAR onto the red–green–blue (RGB) images. As seen in Fig. 5, the proposed model with SC results in highly accurate 3D bounding boxes in all categories.

Table 4. Performance comparison for 3D object detection. APs (in %) for our experimental setup compared with existing leading models.

Method	Data	FPS	Car	Pedestrian	Cyclist

			Easy	Mod.	Hard	Easy	Mod.	Hard	Easy	Mod.	Hard
MV3D	LiDAR + Mono	2.8	71.09	62.35	55.12	-	-	-	-	-	-
F-PointNet	LiDAR +Mono	5.9	81.20	70.39	62.19	**51.21**	44.89	40.23	**71.96**	56.77	50.39
AVOD	LiDAR + Mono	12.5	73.59	65.78	58.38	38.28	31.51	26.98	60.11	44.90	38.80
AVOD-FPN	LiDAR + Mono	10.0	81.94	**71.88**	**66.38**	50.80	42.81	40.88	64.00	52.18	46.61
VoxelNet	LiDAR	4.3	**81.97**	65.46	62.85	57.86	**53.42**	**48.87**	67.17	47.65	45.11
Complex -YOLO	LiDAR	**50.4**	67.72	64.00	63.01	41.79	39.70	35.92	68.17	58.32	54.30
Our model with SC	LiDAR	35.7	71.76	67.43	65.63	47.07	42.53	39.36	69.16	**59.24**	**55.25**
Our model without SC	LiDAR	35.7	68.94	66.65	65.39	38.03	32.43	28.64	58.40	50.61	45.75

(Note: MV3D is from Chen et al. (2017), F-PointNet is from Qi et al. (2017b), AVOD is from Ku et al. (2017), AVOD-FPN is from Ku et al. (2017), VoxelNet is from Chen and Tuzel (2018), and Complex-YOLO is from Simon et al. (2018))

Figure 5. Qualitative results. 3D boxes detected with LiDAR are projected onto the RGB images.

5. Conclusion

Most existing LiDAR-based 3D real-time object detection methods are based on CNN. Although they have achieved high detection accuracy, few works have considered network energy consumption and sparsity. This study is the first to report the development of an SCNN based on the YOLOv2 architecture to detect real-time objects using the KITTI 3D point-cloud dataset. To implement this, we designed a novel data preprocessing layer to translate the 3D point clouds from the KITTI dataset directly into the spike times. The experimental results demonstrate that our proposed network with SC reached

the-state-of-the-art accuracy with the birds-eye-view and full 3D detection. Moreover, in some cases, our proposed network with SC performed better than the others reported in the literature. Considering the support of current processors, we also built another network without SC. Although the network without SC performed slightly worse than that with SC, it still reached state-of-the-art accuracy. These results clearly indicate the effectiveness of the proposed network. In terms of energy consumption and network sparsity, our model only consumed an average of 0.585 mJ with a mean sparsity of 56.24%, indicating higher energy efficiency.

Acknowledgment

This research was partially supported by the National Natural Science Foundation of China (Grant No. 91846301)

References

Chen, X., Ma, H., Wan, J., Li, B., Xia, T. (2017) Multi-view 3D object detection network for autonomous driving. *Proceedings of the IEEE Conference on Computer Vision and Pattern Recognition*, (CVPR), pages 6526–6534.

Engelcke, M., Rao, D., Wang, D. Z., Tong, C. H., Posner. I. (2017) Vote3deep: fast object detection in 3d point clouds using efficient convolutional neural networks. *2017 IEEE International Conference on Robotics and Automation* (ICRA), pages 1355–1361, May 2017.

Geiger, A., Lenz, P., Urtasun, R. (2012) Are we ready for autonomous driving? the KITTI vision benchmark suite. *Proceedings of the IEEE conference on computer vision and pattern recognition*, 128.

Gonzalez, A., Villalonga, G., Xu, J., Vazquez, D., Amores, J., Lopez, A. (2015) Multiview random forest of local experts combining RGB and LIDAR data for pedestrian detection. *2015 IEEE Intelligent Vehicles Symposium* (*IV*), July, Seoul, South Korea.

Girshick, R., Donahue, J., Darrell, T., Malik. J. (2014) Rich feature hierarchies for accurate object detection and semantic segmentation. *Proceedings of the IEEE conference on computer vision and pattern recognition*, pages 580–587.

He, K., Zhang, X., Ren, S., Sun, J. (2015) Deep residual learning for image recognition. *arXiv:* 1512.03385.

Ku, J., Mozifian, M., Lee, J., Harakeh, A., Waslander, S. (2017) Joint 3d proposal generation and object detection from view aggregation. *arXiv*:1712.02294.

Kheradpisheh, S. R., Ganjtabesh, M., Thorpe, S. J., Masquelier, T. (2018) STDP-based spiking deep convolutional neural networks for object recognition. *Neural Networks*, 99, 56–

Mostafa, H. (2018) Supervised Learning Based Temporal Coding in Spiking Neural Networks. *IEEE Transactions on Neural Networks and Learning Systems*. 29(7), 3227-3235.

Merolla, P., Arthur, J., Akopyan, F., Imam, N., Manohar, R., Modha, D. (2011) A digital neurosynaptic core using embedded crossbar memory with 45pJ per spike in 45nm. *2011 IEEE custom integrated circuits conference (CICC)*, San Jose, CA, USA.

Orhan, A. E., Pitkow, X. (2018) Skip connections eliminate singularities. *arXiv*:1701.09175.

Premebida, C., Carreira, J., Batista, J., Nunes, U. (2014) Pedestrian detection combining RGB and dense LIDAR data. 2014 IEEE/RSJ International Conference on Intelligent Robots and Systems, Sept 14-18.

Ponulak, Filip, and Andrzej Kasinski. (2011) Introduction to spiking neural networks: Information processing, learning and applications. *Acta Neurobiologiae Experimentalis* 71(4): 409-433.

Qi, C.R., Su, H., Mo, K., Guibas, L.J. (2016) Pointnet: Deep learning on point sets for 3d classification and segmentation. *arXiv*:1612.00593.

Qi, C.R., Yi, L., Su, H., Guibas, L.J. (2017a) Pointnet++: deep hierarchical feature learning on point sets in a metric space. *arXiv*:1706.02413.

Qi, C.R., Liu, W., Wu, C., Su, H., Guibas, L.J. (2017b) Frustum pointnets for 3d object detection from RGB-D data. *arXiv*:1711.08488.

Redmon, J., Divvala, S.K., Girshick, R.B., Farhadi, A. (2015) You only look once: Unified, real-time object detection. *arXiv*:1506.02640.

Ren, S., He, K., Girshick, R.B., Sun, J. (2015) Faster R-CNN: towards real-time object detection with region proposal networks. *arXiv*: 1506.01497.

Simon, M. Milz, S., Amende, K., Gross, H. M. (2018) Complex-YOLO: Real-time 3D object detection on point clouds. *arXiv: 1803.06199.*

Simon, M., Amende, K., Kraus, A., Honer, J., Gross, H. M. (2019) Complexer-YOLO: Real-time 3D object detection and tracking on semantic point clouds. *arXiv*:1904.07537.

Tavanaei, A., Ghodrati, M., Kheradpisheh, S. R., Masquelier, T., Maida, A. (2019) Deep learning in spiking neural networks. *Neural Networks*, 111, 47-63.

Wang, D. Z., Posner, I. (2015) Voting for voting in online point cloud object detection. In Proceedings of Robotics: Science and Systems, Rome, Italy, July.

Zhou, S., Chen, Y., Ye, Q., Li, J. (2019) Direct training based spiking convolutional neural networks for object recognition, *arXiv*: 1909.10837.

Zhou, Y., Tuzel, O. (2018) VoxelNet: end-to-end learning for point cloud based 3D object detection. *2018 IEEE/CVF Conference on Computer Vision and Pattern Recognition*, Jun 18-23, Salt Lake City, UT, USA.